Solidification and microstructure modelling of welds in aluminium alloys 5754 and 6111

S. S. Babu, S. A. David, J. M. Vitek, and R. W. Reed

A solidification and microstructure modelling approach has been developed to predict weld metal and heat affected zone (HAZ) characteristics. The freezing range and phase evolution in the weld metal region were predicted using thermodynamic and diffusion controlled growth calculations. The calculated freezing range was correlated with the weld solidification cracking tendency. A simplified analytical model was suggested to describe thermal cycles that are experienced by the HAZ. This analytical model was coupled with a published microstructure model for age hardenable alloys to predict the hardness variations across the HAZ. The above integrated approach was evaluated using experimental welds made on non-age hardenable 5754 (Al–Mg) and age hardenable 6111 (Al–Mg–Si) alloys using gas tungsten arc, electron beam, and gas metal arc welding processes.

The authors are in the Metals and Ceramics Division, Oak Ridge National Laboratory, Oak Ridge, TN 37831–6096, USA. *Manuscript received 1 March 2000; accepted 26 May 2000.*

INTRODUCTION

New initiatives to reduce the weight of vehicles and thereby to increase fuel efficiency have led to the consideration of aluminium alloys for automotive structural applications.[1] Alloys of interest are age hardenable Al–Mg–Si alloy 6111 and non-age hardenable Al–Mg alloy 5754.[2,3] In addition to high strength, these alloys must exhibit good weldability.[4,5] The weldability criteria include resistance to weld solidification cracking, good performance during service, and the ability to achieve consistent properties over a wide range of welding processes and process parameters. Also, higher productivity necessitates increased welding speeds. To fulfil these requirements, researchers have focused on the application of various welding processes such as laser welding[4] and high speed gas metal arc (GMA) welding,[6] and the development of hybrid welding processes that combine the advantages of arc and laser welding.[7,8] However, to optimise welding process parameters and achieve the desired weld properties, extensive trial and error experimentation is necessary. An alternative approach is to develop an integrated process model that can predict weld properties as a function of alloy compositions, welding processes, and process parameters.

The present paper describes a methodology that will aid in the optimisation of welding processes, and process parameters and properties, for aluminium alloys. The critical elements of this process model include predictions of weld pool shape, weld thermal cycle, and weld metal (WM) and heat affected zone (HAZ) microstructures, as shown in Fig. 1. The approach presented uses experimental weld pool shape measurement, an analytical model for weld thermal cycles, and a numerical model for WM and HAZ microstructures.

MODEL DEVELOPMENT

Model for HAZ thermal cycle predictions

In general, predictions of HAZ thermal cycles have been carried out using analytical models[9–14] and numerical models.[15–18] Each of these approaches has merits and limitations.

Analytical models rely on the solution of quasistationary heat transfer equations. These equations have been modified to include heat source geometry and arc efficiencies to predict simple weld pool geometry and thermal cycles. Recent work has focused on extending these equations to laser processing.[14] The original equation for quasistationary temperature distribution for thick plates as a function of radial distance from the arc r and time t is given by[12]

$$T\{r,t\} = T_0 + \frac{\eta(q/v)}{2\pi\lambda t}\exp\left(-\frac{r^2}{4at}\right) \quad \ldots\ldots (1)$$

and for thin plates is given by

$$T\{r,t\} = T_0 + \frac{\eta(q/v)}{d(4\pi\lambda\rho ct)^{1/2}}\exp\left(-\frac{r^2}{4at}\right) \quad \ldots\ldots (2)$$

where η is the arc efficiency, d is the thickness of sheet, q is the arc power, v is the welding speed, λ is the thermal conductivity, a is the thermal diffusivity, ρc is the specific heat per unit volume, and T_0 is the preheat temperature before welding. Although these equations have been used extensively to predict simple weld pool shapes and thermal cycles for conventional welding processes, modified arc efficiencies η' are required for prediction of weld pool shape and thermal cycles. This approach has limitations because of the inability of analytical heat transfer equations to describe complex weld pool shapes caused by fluid flow conditions in the weld.[18] The analytical model ignores

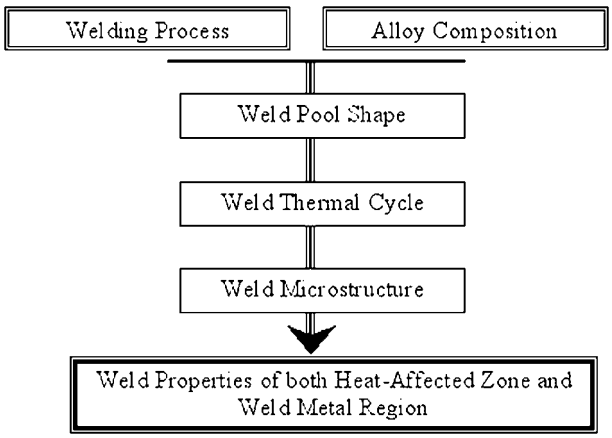

1 Process model requirements that must be addressed by integrated welding process model

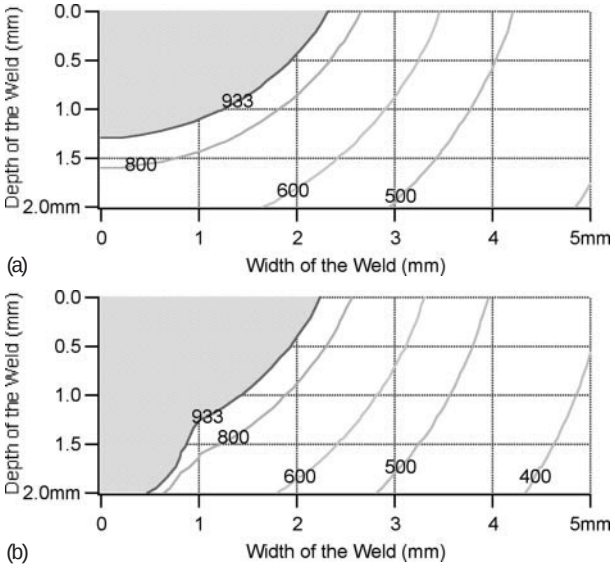

a one heat source with 0·001 m radius on surface of sheet; *b* additional virtual spherical heat source just below surface of sheet at 0·0014 m depth and with time delay of 0·0005 s with respect to surface heat source

2 Typical calculations of weld pool shape and predicted size for gas tungsten arc (GTA) welding of 6111 alloy at 12 V, 110 A, and 0·02117 m s^{-1}

convective heat transfer, and is therefore not capable of accurately predicting a realistic weld pool shape. Extensive analytical calculations on gas tungsten arc (GTA) and electron beam (EB) weld pool shapes (described below) to fit parameters describing the weld pool shape proved futile and often computer intensive.

The second approach is to use numerical models that describe both conductive and convective heat transfer in welds.[15–18] These models provide a more fundamental understanding of the various factors that affect weld pool shape. However, this approach is often complicated by thermophysical property data requirements, arc–plasma interactions, the effect of metal transfer from the arc, and excessive computational times. Therefore, this approach is still far from being able to predict weld pool shape and thermal cycle as a function of process parameters effectively and without extensive trial and error calculations.

In the present work, two analytical approaches were used to predict thermal cycles for a wide range of welding processes and process parameters. First, an analytical equation (equation (2)) and the parameters that describe heat distribution and efficiency are modified to fit the experimentally observed weld pool shape. The complex weld pool shape was handled by placing a virtual spherical heat source just below the surface of the sheet in addition to the usual heat source on the surface of the sheet (Fig. 2) and by modifying its characteristics. The calculations replicate the fluid flow effects. However, extensive calculations with changes in placement and power distribution characteristics between main arc and virtual heat source below the surface were found to give arbitrary results. As a result, a generalised method could not be developed. In addition, different ellipsoidal heat source geometries were considered, similar to the approach of Goldak *et al.*;[19] however, these were also unsuccessful.

In the second approach, after obtaining the fusion boundary profile from experimental measurements, the aluminium alloy sheet being analysed was considered as a composite of stacked virtual thin sheets. Equation (2) was then used to estimate the effective value of $\eta(q/v)$ for each virtual sheet that satisfied the experimentally measured weld

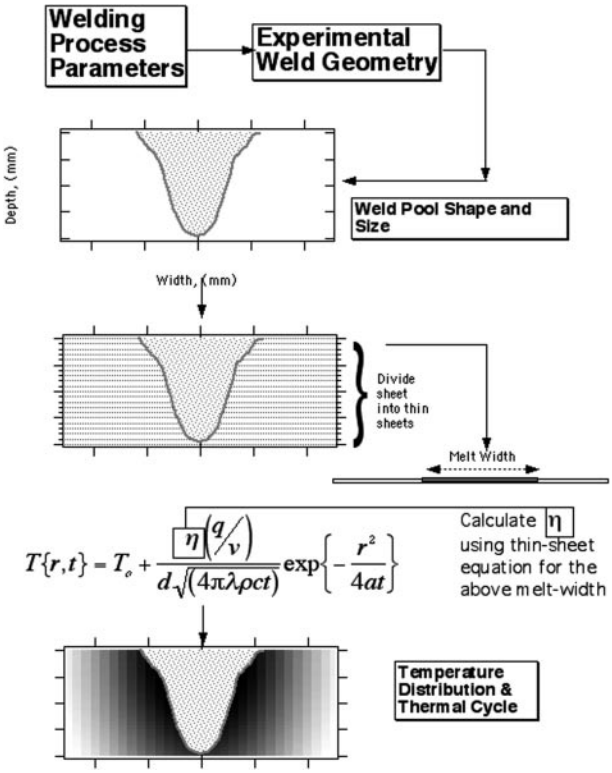

3 Methodology for calculating temperature distribution in aluminium alloy sheets

pool width, and the HAZ thermal cycles along the width of this virtual sheet were calculated. This approach was repeated for all virtual thin sheets. An inherent condition in this approach is that heat transfer occurs only along the width of the sheets and not through the thickness of the sheets. Note that this condition is not valid in real welds, which exhibit partial penetration. However, this method was simple and computationally less intensive and can be applied for full penetration welds. This approach, explained schematically in Fig. 3, has inherent advantages: it can be applied to any welding process, any set of welding process parameters, and any material, provided that the weld pool profile and the thermophysical properties of the material under analysis are known. This method is also suitable for coupling with artificial neural network models for weld pool shape.

Microstructure models

Model for weld metal microstructure

Previous microstructure models have considered HAZ softening.[20–24] However, none of these process models considered the weld metal (WM) region. Therefore, the present work has focused on developing a methodology to describe the microstructure evolution in the WM region. However, the modelling efforts in this paper are restricted to the prediction of phase evolution and the freezing range, and will be based on thermodynamic calculations as well as diffusion controlled solidification simulations; these are explained briefly below.

In aluminium alloys, the solidification microstructure consists of the primary solid solution α phase and the eutectic phase.[25] Inherent in the process of solidification is the partitioning and redistribution of alloying elements. For binary systems, the solidification process can be described using phase diagrams.[26] However, for ternary and other higher order systems, it is necessary to rely on experimental measurements or multicomponent equilibrium thermo-

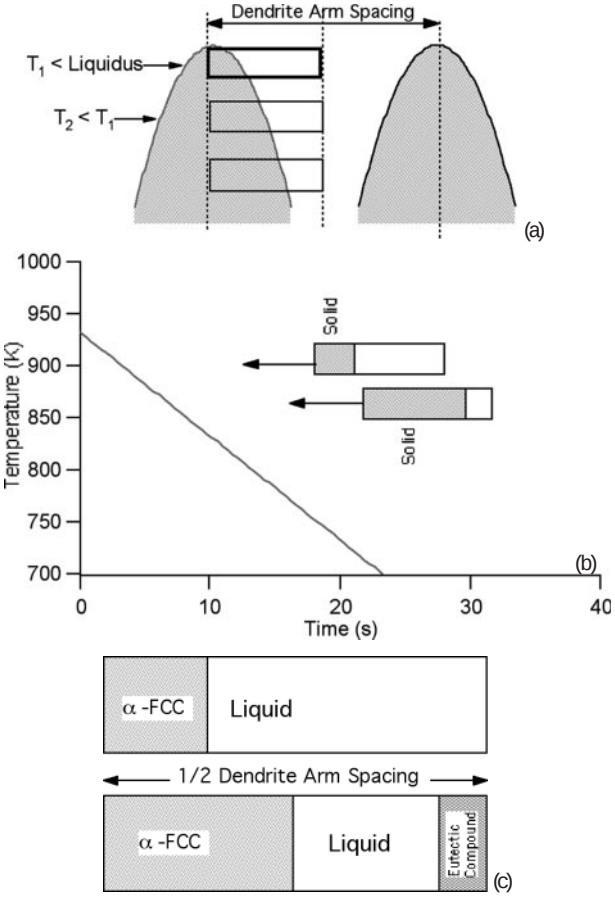

a dendrite region considered for diffusion controlled solidification simulation – calculations assume no temperature gradient perpendicular to dendrite growth direction and consider diffusion within α-fcc and liquid phase; *b* schematic illustrations of weld cooling curve and extent of solidification; *c* schematic illustration of diffusion geometry to allow for eutectic compound precipitation during final stages of solidification from enriched liquid – in this condition geometry allows for simultaneous growth of α-fcc phase from left and growth of eutectic compound from right

4 Geometry of diffusion controlled solidification simulation

dynamic calculations.[27] Using these calculations and the Scheil additivity rule, the sequence of phase evolution during weld solidification can be predicted. Such calculations can describe the variations of solid fraction and the extent of eutectic phase formation as a function of temperature. The details of the calculation can be found in Ref. 28. However, this method cannot describe the effects of the weld cooling rate because it ignores diffusion effects.

The second approach was to incorporate the weld cooling rate effects by considering diffusion controlled growth of the α phase in the liquid. This can be achieved by assuming local equilibrium at the moving solid/liquid interface and numerically solving the diffusion flux equations in the α and liquid phases. The interface velocity is controlled by local equilibrium at the interface and mass balance criteria relating to the flux across the interface. Such calculations can be performed using commercially available kinetic software such as DicTra.[29,30] To describe the α phase growth, a small volume element equivalent to the half dendrite arm spacing (HDAS) was defined, as shown in Fig. 4*a*. In addition, a linear cooling rate was assumed in the weld pool, as shown in Fig. 4*b*. It was also assumed that the eutectic compound phase growth starts from the right hand edge of the volume element (Fig. 4*c*).

Model for HAZ microstructure

For age hardening alloys, it is necessary to consider coarsening and possible dissolution during heating as well as precipitation during cooling in the HAZ regions. For non-age hardenable alloys, only the grain growth is of interest.

For the age hardenable Al–Mg–Si alloy, it is important to describe the combination of dissolution and precipitation reactions during a thermal cycle.[20–24] The present work has adopted the model developed by Myhr and Grong.[21,22] In this model, kinetic equations describe the dissolution and precipitation of β'' (Mg_2Si) precipitates. The dissolution equation is related to the activation energy for magnesium diffusion and metastable solvus boundary (β'') enthalpy. The extent of dissolution is used to predict the extent of softening (or hardness reduction). The precipitation reaction is related to the supersaturation of solutes required for precipitation of β'' and to the formation of non-hardening equilibrium β' precipitates. The extent of precipitation is then used to predict the extent of hardening (or hardness increase). The details of this model can be obtained from Refs. 21 and 22.

In the present work, the HAZ thermal cycle predicted via the method described above was divided into small isothermal steps at various temperatures. The extent of softening and hardening is calculated for each step. By assuming the additivity rule, the overall extent of softening and hardening was then calculated by numerical integration. This approach was repeated for all the locations to obtain the hardness distribution throughout the HAZ.

For the non-age hardenable alloy, analytical models or Monte Carlo simulations can be used to describe grain growth.[13,31] Because no appreciable grain growth was observed for the alloy considered in the present investigation, detailed modelling was not attempted.

EXPERIMENTAL PROCEDURE

Heat treatable Al–Mg–Si (6111) and non-heat treatable Al–Mg (5754) alloys were considered in the present study. For GMA welding, Al–Si (4047) and Al–Mg (5554) filler metals were used for the 6111 and 5754 alloys, respectively. The compositions of these alloys are given in Table 1. The 6111 alloy was used in the form of 2 mm thickness sheets in the T4 (solution treated and naturally aged) condition. The 5754 alloy was 3 mm in thickness and in the annealed condition. Welds were produced using GTA, GMA, and EB welding processes. The welding parameters used are given in Table 2. The GTA and EB welds were made via the autogenous bead on plate technique. To avoid cracking during EB welding, beam oscillation was used with circle generation. For GMA welding, a butt joint geometry with a gap range from 0·5 to 0·8 mm was used. Microstructural characterisation of the weld was performed using conventional metallographic techniques and optical microscopy. The weld samples were examined in both the longitudinal and transverse directions. The samples were then etched in modified Keller's reagent (95 mL H_2O, 1 mL HCl, 1·5 mL HF, and 2·5 mL HNO_3). The spatial hardness distributions in the welds were measured using an automated hardness tester with a load of 100 g. Tensile properties of welds were measured in an instrumented Instron universal testing

Table 1 Nominal composition of alloys studied, wt-%

Description	Alloy	Si	Cu	Mn	Mg	Al
Age hardenable alloy	6111	0·85	0·70	0·27	0·75	Bal.
Non heat treatable alloy	5754	…	…	0·30	3·10	Bal.
Filler wire for 6111	4047	12	…	…	…	Bal.
Filler wire for 5754	5554	…	…	0·80	2·7	Bal.

machine with a crosshead speed of 0·03175 mm s^{-1}. In the tensile test sample, the weld was oriented perpendicular to the tensile stress axis and was in the middle of the gauge length. The samples had an overall length of 102 mm, a gauge length of 32 mm, and a width of 6·35 mm. The geometry of the test samples was constant and care was taken to avoid any reinforcement that had been introduced because of welding. In addition, care was taken not to test the samples with hot cracks or any other physical defects that could be detected using an optical microscope.

RESULTS AND DISCUSSION

Alloy 5754 weld microstructure and properties

Successful autogenous (without filler wire) bead on plate welds were obtained using the GTA and EB welding processes. In addition, successful butt joints were produced using the GMA welding process and 5554 filler metal. Examination of the welds revealed significant differences in weld pool shape and size as a function of welding process. The GMA welds revealed some indication of porosity and this is attributed to insufficient shielding during welding. Microstructural observations in the HAZ, in both GTA and EB welds, showed negligible changes in grain size (Fig. 5). This observation was also consistent with GMA welds. However, significant microstructural differences were found in the WM region in the welds produced by different processes. The WM region exhibited a dendritic solidification structure with eutectic constituents in the interdendritic regions. The dendrite arm spacing was found to be smaller in EB welds (2–5 μm) than in GTA or GMA welds (5–20 μm), as shown in Fig. 6. This reduction in dendrite arm spacing is related to more rapid cooling rates in the EB welds.[32]

The hardness values measured across the weldment failed to show any significant differences between WM, HAZ, and base metal. Tensile properties were measured for 5754 alloy weldments produced by GTA and GMA welding processes. The measured offset yield strength, ultimate tensile strength, and ductility values are compared with those of the base metal in Fig. 7. The results show that there is no significant difference between the tensile properties of the welds and the base metal. Moreover, most of the failures occurred in the base metal region. This shows that the transverse properties of 5754 welds are insensitive to the welding process and changes in the process parameters. However, there may be changes in properties along longitudinal directions and it is expected that under high welding heat input conditions soft zones may develop in the HAZ as a result of grain growth; these were not encountered in the present work.

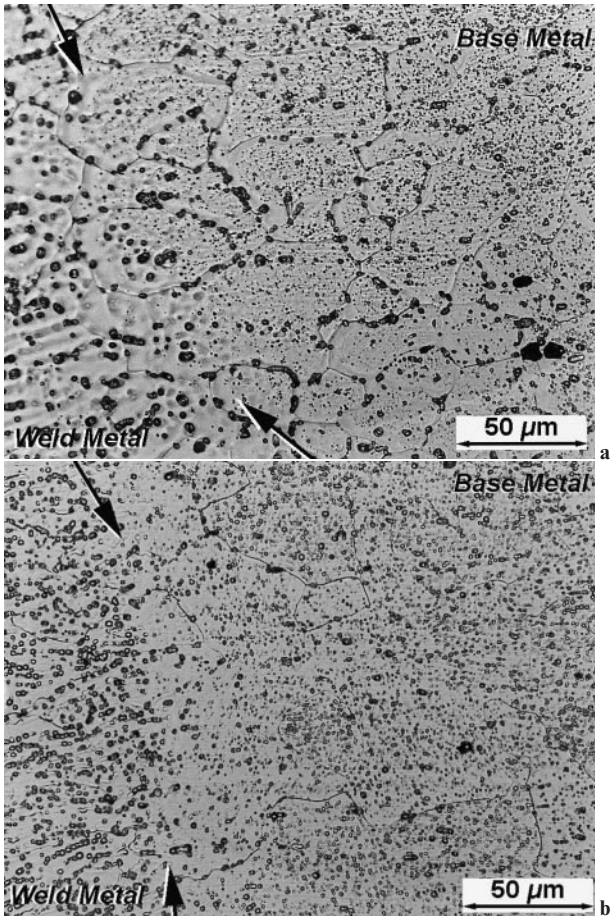

5 Comparison of heat affected zone (HAZ) microstructure from 5754 welds produced using *a* GTA and *b* electron beam (EB) welding processes: arrows and lines mark boundary between weld metal and HAZ regions (optical)

Table 2 Welding process parameters used in present study

Welding process	Alloy	Voltage, V	Current, A	Speed, mm s^{-1}	Circle generator, Hz	Shielding gas	Wire feedrate, mm s^{-1}	Heat input,* kJ m^{-1}
EB	6111	60×10^3	$16{\cdot}5 \times 10^{-3}$	21·17	10 (coarse) 3 (fine)	…	…	46·7643
	6111	60×10^3	$19{\cdot}0 \times 10^{-3}$	42·34	10 (coarse) 3 (fine)	…	…	26·9249
	5754	60×10^3	$19{\cdot}0 \times 10^{-3}$	21·17	10 (coarse) 5 (fine)	…	…	53·8498
	5754	60×10^3	$26{\cdot}5 \times 10^{-3}$	42·34	10 (coarse) 5 (fine)	…	…	37·5531
GTA	6111	12	110	21·17	…	Helium	…	62·3524
	6111	12	180	42·34	…	Helium	…	51·0156
	5754	12	175	21·17	…	Helium	…	99·197
	5754	12	265	42·34	…	Helium	…	75·1063
GMA	6111†	21·0	110	21·17	…	Argon	127	109·117
	6111†	22·5	180	42·34	…	Argon	212	95·6542
	5754‡	21·5	165	21·17	…	Argon	222	167·572
	5754‡	23·0	215	42·34	…	Argon	307	116·793

*Heat input = (voltage × current)/welding speed.
†Welded using 0·9 mm diameter 4047 filler wire.
‡Welded using 0·9 mm diameter 5554 filler wire.

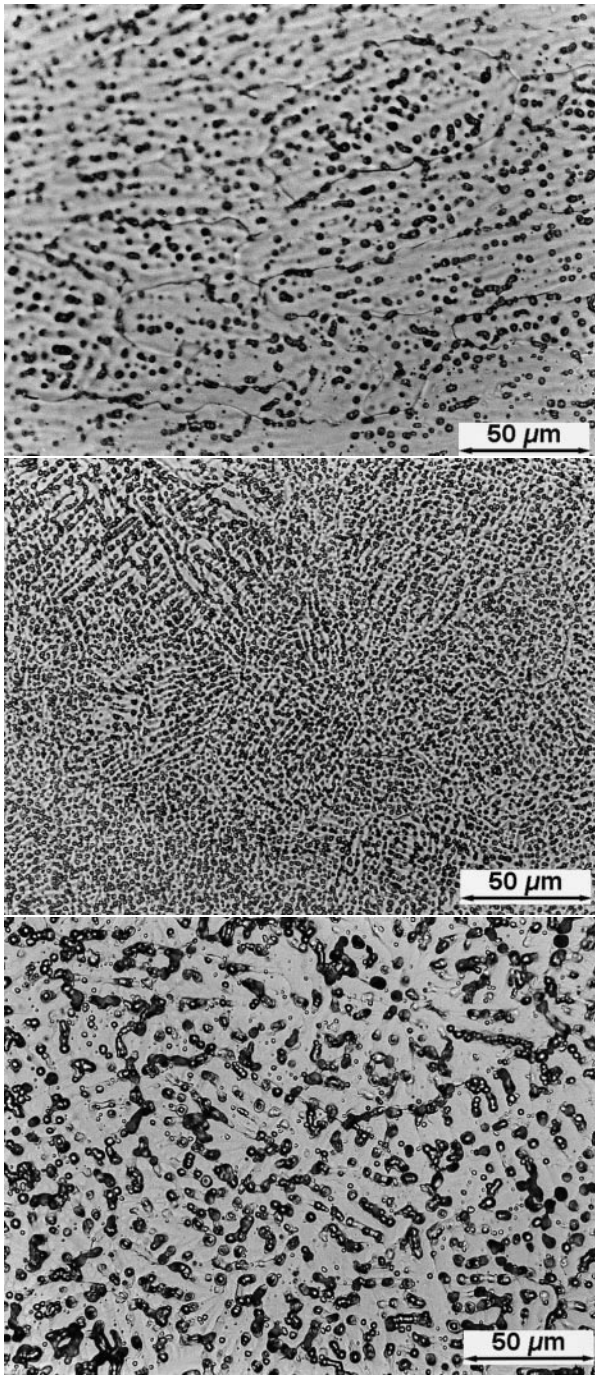

6 Comparison of weld metal (WM) microstructure in 5754 welds produced via *a* GTA welding, *b* EB welding, and *c* gas metal arc (GMA) welding with 5554 filler wire (optical)

Alloy 6111 weld microstructure and properties

During GTA welding of the 6111 alloy, although crack free welds were produced over short sections, significant cracking was observed in most of the welds. This is consistent with previous observations.[5] The weld solidification cracking in this alloy can be related to the extended solidification temperature range.[33–35] As mentioned above, EB welds were made with beam oscillation to avoid weld cracking. Crack free welds were produced in the 6111 alloy using this process modification. The beam oscillations are expected to change the thermal conditions near the solid/liquid interface, and the grain structure.[32] The GMA welding process was used with 4047 filler material to produce butt joints in the 6111 alloy without weld solidification cracking. This is attributed to the large concentrations of silicon in the 4047 filler wire and this is also consistent with previous observations.[5]

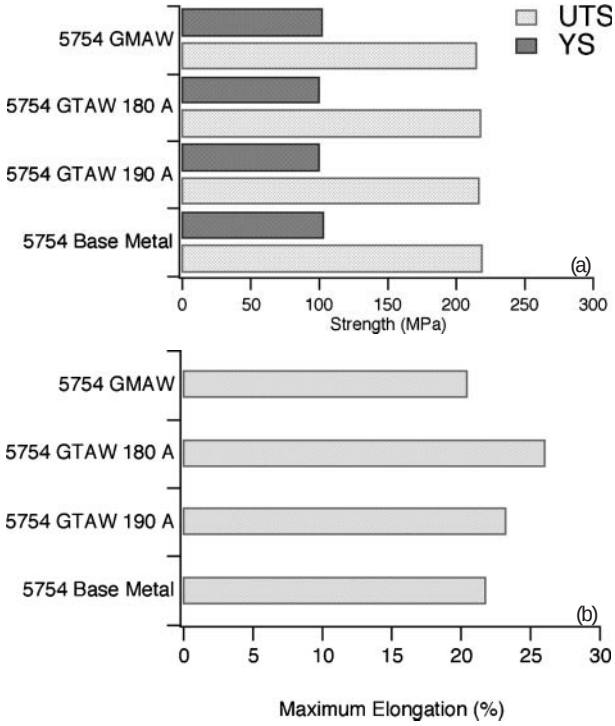

a ultimate yield strength (UTS) and yield strength (YS); *b* ductility

7 Tensile properties of 5754 welds

The HAZ microstructures for GTA, EB, and GMA welding of 6111 alloy are compared in Fig. 8. The HAZ of the welds showed coarse precipitates within the grains and precipitate free zones near the grain boundary (indicated by an arrow). The extent of this HAZ was small in EB welds compared with that in GTA and GMA welds. The WM microstructures of all the welds are compared in Fig. 9. The welds exhibited a dendritic solidification substructure. The dendrite arm spacing was found to be finer for EB weld metals and much coarser for both GTA and GMA welds. In addition, eutectic constituent was observed in the interdendritic regions of all welds.

Hardness across the weldment region was measured for all the welds. The spatial hardness distributions show evidence of HAZ softening (Fig. 10). Analysis of the hardness distributions showed that the width of the HAZ in EB welds was found to be smaller than that in GTA and GMA welds. The WM region of GMA welds showed a higher hardness because of the 4047 filler wire, and some degree of scatter. This may be due to a local change in the solidification substructure. In autogenous GTA and EB welds, the WM region showed a hardness of 50–60 HV0·1, and the variation within the WM region was found to be very small. In all the welds investigated in the present work, the hardness of the WM region was found to be lower than that of both the HAZ and base metal regions. This is expected to have an effect on the tensile properties of the weldment. During tensile testing of the GMA welds, all failures occurred consistently in the WM region (yield strength YS = 143 ± 2·8 MPa, ultimate tensile strength UTS = 251·7 ± 7·1 MPa, and total elongation of 7·9 ± 1·5%), indicating that this region is the weakest when compared with the values for the base metal (YS = 179·4 ± 2·8 MPa, UTS = 308·5 ± 1·8 MPa, and total elongation of 25 ± 2·8%).

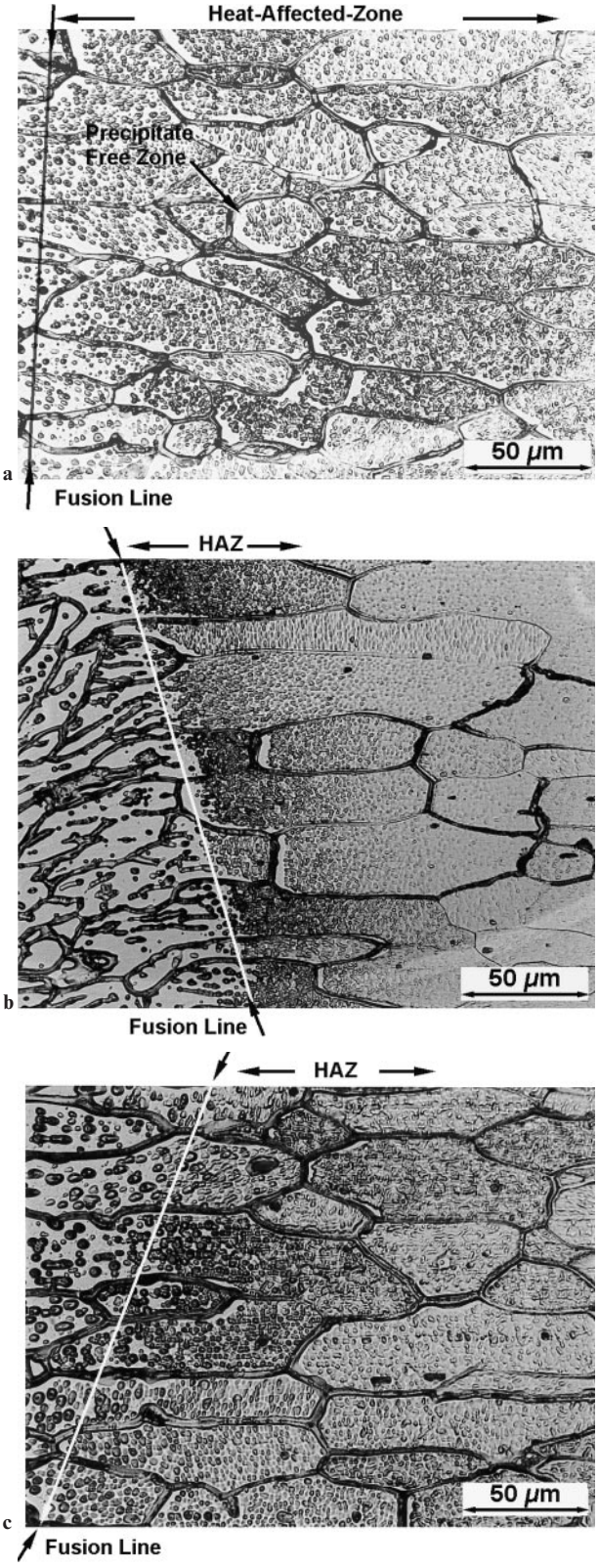

8 Comparison of HAZ microstructure from 6111 welds produced via *a* GTA, *b* EB, and *c* GMA welding processes: arrows mark fusion zone boundaries (optical)

Based on these results, it can be concluded that the 6111 alloys are sensitive to the welding process and the joint properties are inferior to those of the base metal. Therefore, further work is required to enhance the WM properties by using appropriate filler metal compositions or process modifications that would significantly alter the microstructural features. Since the properties of the 6111 alloy WM region show a possible dependency on composition and cooling rate, microstructure models are necessary for optimisation of 6111 alloy welding.

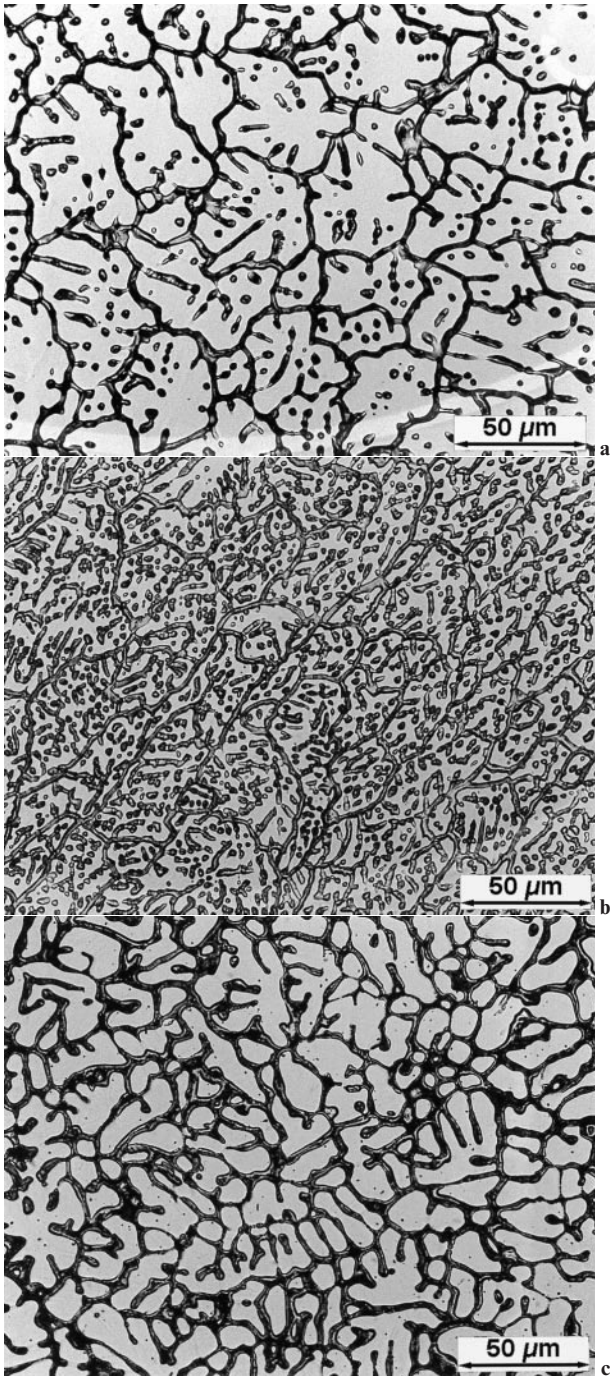

9 Comparison of WM microstructure from 6111 alloy welds produced via *a* GTA, *b* EB, and *c* GMA welding processes (optical)

MICROSTRUCTURE MODELLING OF 6111 ALLOY WELDS

Weld metal microstructure

To define the microstructural features and cracking sensitivity of the 6111 alloy welds, it is critical to understand the phase evolution and the freezing range during weld solidification, respectively.

Equilibrium thermodynamic calculations were carried out for 6111 and 4047 alloys to establish the effects of

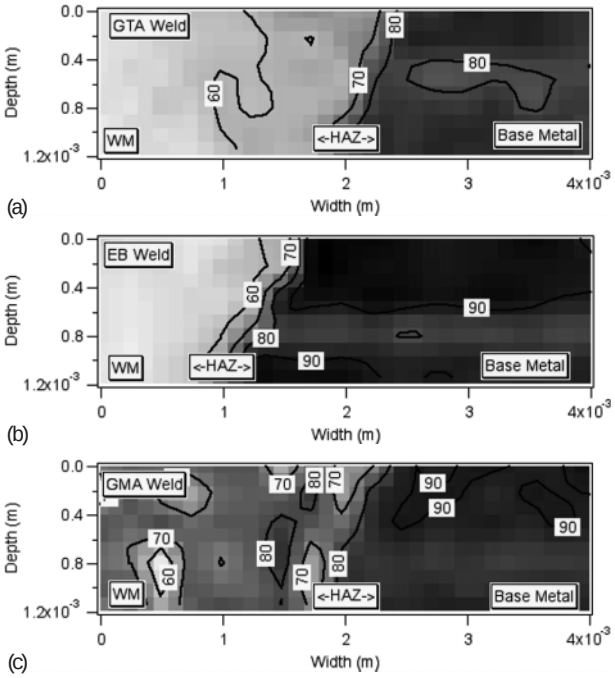

10 Spatial hardness distribution across weld region shown in form of image and contour plots for *a* GTA, *b* EB, and *c* GMA welds

alloying elements on phase evolution. The elements that are considered in this calculation are copper, iron, magnesium, manganese, silicon, and titanium, and the phases that are considered include α solid solution phase, pure silicon, Al_2Cu, Al_6Mn, AlCuFeMnSi phase, $Al_8FeMg_3Si_6$, Al_3Mg_2, $Al_5Cu_2Mg_8Si_6$, and Mg_2Si. Using the Scheil additivity rule, liquid fraction variation with temperature was calculated and is shown in Fig. 11. The plot shows a large freezing range for the 6111 alloy compared with that of 4047 and it shows the formation of numerous phases during cooling. This large freezing range in the 6111 alloy will increase the hot cracking tendency during autogenous welding.[5,33–35] This is supported by the observed hot cracking tendency of the 6111 alloy. The results of these calculations are significant in that they consider multicomponent and multiphase thermodynamic equilibria and relate them to experimentally observed hot cracking phenomena. An approach to mitigate the hot cracking problem is to use a suitable filler metal composition that would freeze over a narrow range of temperature. The calculation in Fig. 11*b* shows that 4047 filler metal solidifies over a small temperature range, and the experimental welds showed no cracking when alloy 6111 was welded using 4047 filler metal. These results show that basic equilibrium thermodynamic calculations can be used to predict the susceptibility of alloys to weld solidification cracking.

The calculations also enabled the prediction of which phase forms as the weld pool cools (Fig. 11). For the 6111 alloys, 80% of the solidification involves formation of primary α phase. The solidification start temperature was 924 K. As solidification progresses, various intermetallic phases start to precipitate. The sequence of phase formation is shown in Fig. 11*a*. However, in casting practice, only Mg_2Si precipitation has been observed. This may be attributed to kinetics of solidification, which was neglected in the calculations. Efforts are in progress to carry out high resolution transmission electron microscopy and phase identification to resolve this difference. In contrast to the 6111 alloys, in 4047 alloys, 5% of the initial solidification occurs by the formation of primary α phase and the rest by eutectic decomposition of liquid to α + silicon.

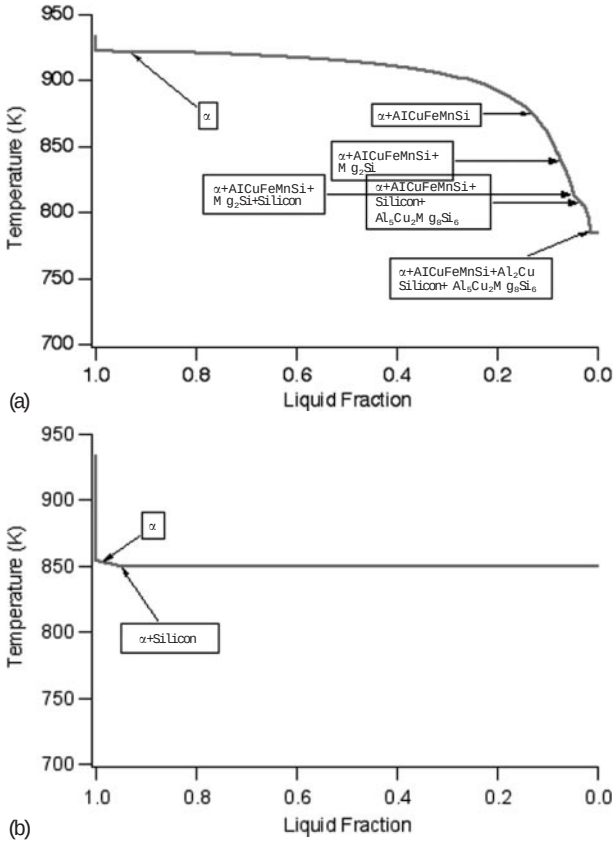

11 Phase evolution using Scheil additivity rule for *a* 6111 and *b* 4047 (filler alloy)

As stated previously, the present results ignored kinetic considerations. Therefore, diffusion controlled growth calculations were made to incorporate the kinetic effects. The geometry of the diffusion controlled solidification simulation is shown in Fig. 4. Before applying this methodology to 6111 and 4047 aluminium alloys, it was evaluated by comparison with experimental data for the Al–Mg system,[25] with similar cooling rates having been employed in those experiments. The measured solidification curves from differential thermal analyses and interrupted quenching experiments compared well with calculations.[36] Appropriate consideration of the cooling rates and dendrite arm spacing in diffusion controlled solidification simulations is important.

Having verified the methodology, the calculations were applied to evaluate solidification characteristics in 6111 and 4047 aluminium alloy welds. For the 6111 aluminium alloy, the calculations permitted consideration of only one eutectic phase, namely, Mg_2Si. The simulations followed the liquid/primary α phase interface and liquid/Mg_2Si interface positions as a function of time for a given cooling rate. The diffusion controlled solidification simulations were performed for different cooling rates ($1-10\,000$ K s^{-1}) and different HDAS (half dendrite arm spacing) values. Note that these calculations do not consider the nucleation condition and heat transfer conditions that usually determine the HDAS value. As a result, two different cases were defined: for case 1, the HDAS was fixed at a constant value, whereas for case 2, the HDAS values were varied as a function of weld cooling rate (Fig. 12). The rationale behind using high cooling rates in the present work was to evaluate the solidification conditions that may be experienced by aluminium alloys during pulsed laser welding conditions. It is important to note that this work does not consider dilution effects. This may be significant in high heat input welds. Since the focus

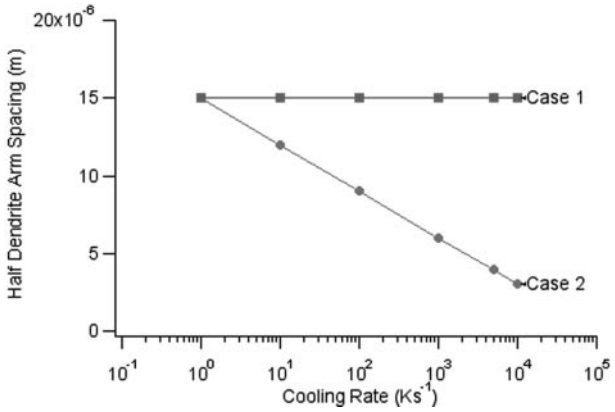

12 Assumed variations of half dendrite arm spacing with cooling rate (cases 1 and 2) considered in diffusion controlled simulations

of the present work was to establish the modelling methodology, the effective dilution in different processes was not considered. An additional assumption in the following calculations is ignorance of the dendrite tip undercooling. This is expected to play an important role at high cooling rates, where the solid/liquid interface may be rapidly cooled to temperatures far below the equilibrium solidification start temperatures.

For all cases, the 6111 alloy began to solidify as primary α phase, and towards the final stages of solidification, the Mg_2Si phase precipitated. The variation of solid fraction with temperature for the two cases and at different cooling rates is shown in Fig. 13. The results show that the variation

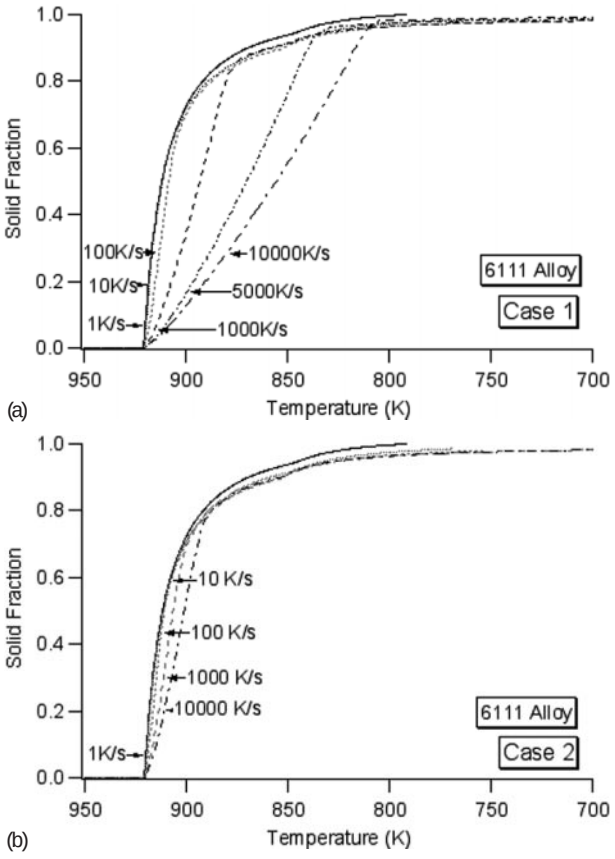

a case 1; *b* case 2

13 Variation of solid fraction with temperature for two diffusion controlled simulation cases (*see* Fig. 12) in 6111 alloy weld

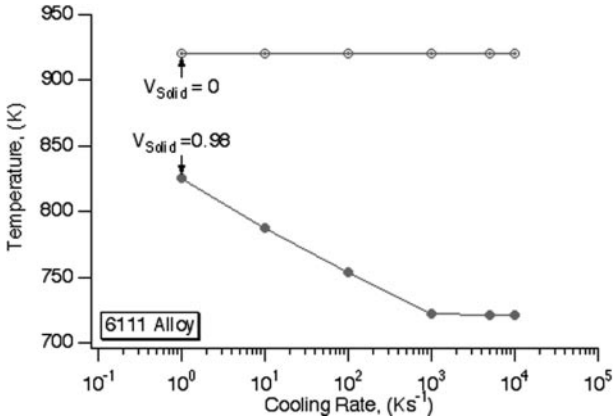

14 Comparisons of solidification start and completion temperatures for alloy 6111 as function of cooling rate, with assumed variation of dendrite arm spacing as given by case 2 in Fig. 12

of solid fraction with temperature is sensitive to the cooling rate only when the HDAS values are fixed at 15 μm (*see* Fig. 13*a*). In this case, as the weld cooling rate increases, the fraction of liquid that remains at lower temperature increases. However, it is well known that as the weld cooling rate increases, the dendrite arm spacing decreases,[32] as can be seen in Fig. 9. Therefore, the results in Fig. 13*a* may differ from real weld solidification conditions and the changes in HDAS must be considered. This condition is considered in case 2 and the resulting variation of solid fraction with temperature is shown in Fig. 13*b*.

The results are markedly different from those for a constant HDAS condition. The solid fraction at lower temperatures increased at lower rates for higher weld cooling rates in the early stages of solidification ($<80\%$). Such a variation is expected, because the diffusion controlled growth rate of the primary α phase will be controlled to a large extent by the overlap of diffusion fields (also referred to as soft impingement) in the liquid. In addition, these variations can also be influenced by the assumed HDAS value. The results from the preceding calculations can be used to extract the freezing range. For this, the solidification completion temperature is taken as the temperature T_{98} at which the volume percentage of solid reaches 98%. This is the limit above which the liquid is enriched and is unable to undergo the instantaneous eutectic decomposition. This analysis shows that, for most of the conditions, a rapid weld cooling rate increases the freezing range (Fig. 14) and will therefore increase hot cracking sensitivity. This is indeed supported by the hot cracking tendencies in EB welds. As discussed above, the present calculations require further improvement to consider dendrite tip undercooling effects and also the effect of dilution from the base metal.

For the 4047 weld metal, the Al–Si alloy system was considered in terms of liquid, primary α, and silicon phases. For 4047 alloys, the eutectic compound was assumed to be silicon. Calculations were performed for 4047 alloys for two conditions. In the first condition, the HDAS was taken as 15 μm with a weld cooling rate of 10 K s^{-1}, and in the second condition, the HDAS was taken as 0·1 μm with a cooling rate of 1000 K s^{-1}. These values are selected to consider extreme conditions. The variation of solid fraction with temperature for these two conditions is shown in Fig. 15. The calculations show that for the 4047 alloy, 10% eutectic silicon phase would form during weld cooling. This is in agreement with the experimental observations from GMA welds. Comparison of the two conditions shows some interesting observations. For the higher weld cooling rate (*see* Fig. 15*b*), the weld solidification is complete at 850 K.

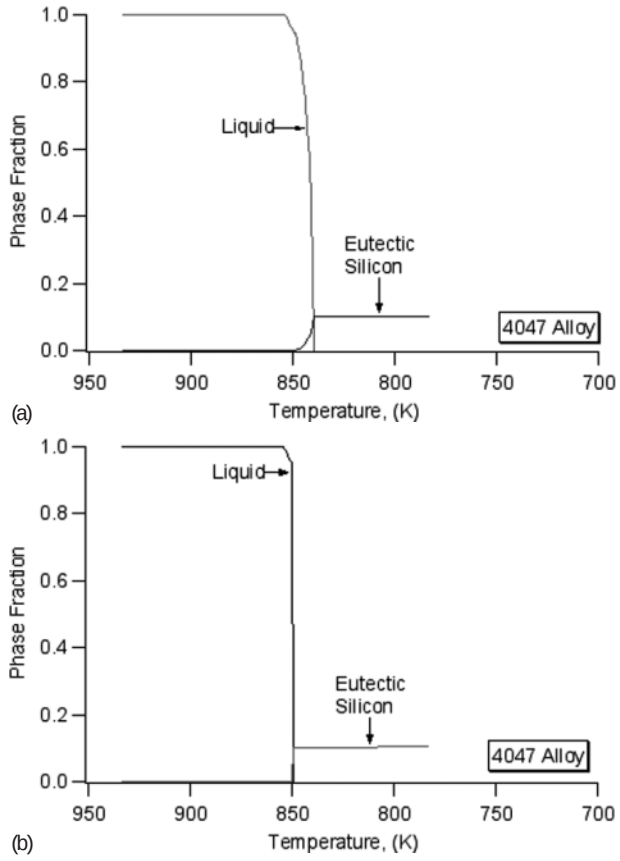

15 Variation of liquid and eutectic silicon fractions with temperature for *a* 10 K s^{-1} cooling rate with 15 μm dendrite arm spacing and *b* 1000 K s^{-1} cooling rate with 0·1 μm dendrite arm spacing for 4047 alloy composition

For the low weld cooling rate, the weld solidification is completed at 840 K. This apparent difference is attributable to the effective enrichment of liquid with silicon in the two conditions. In both instances, the 4047 alloy has a narrow freezing range and therefore shows no cracking tendency. The significance of a 10 K difference in solidification temperature range requires evaluation for different welding processes having large differences in the heat input, which may lead to totally different stress states around the weld and thereby promote weld solidification cracking in such welds.[37] A cautionary note in the above calculations is the validity of the assumed dendrite arm spacing in the predictions. Nevertheless, the diffusion controlled growth simulations can be used to identify crucial parameters that determine trends in weld metal microstructure development. Further work is necessary to relate this microstructure to weld metal properties.

HAZ hardness distribution

The coupled thermal–microstructure model developed for the HAZ was applied to determine the hardness distributions in the weldment. A typical calculation for a GTA weld of the 6111 alloy is shown in Fig. 16. For this calculation, experimental weld pool geometry data were used. The steps in the calculation are as follows.

1. The weld pool geometry, in terms of x and y coordinates, was extracted from the experimental macrostructure (Fig. 16*a*).

2. Using the thermal model described above, the maximum temperatures across the HAZ were predicted

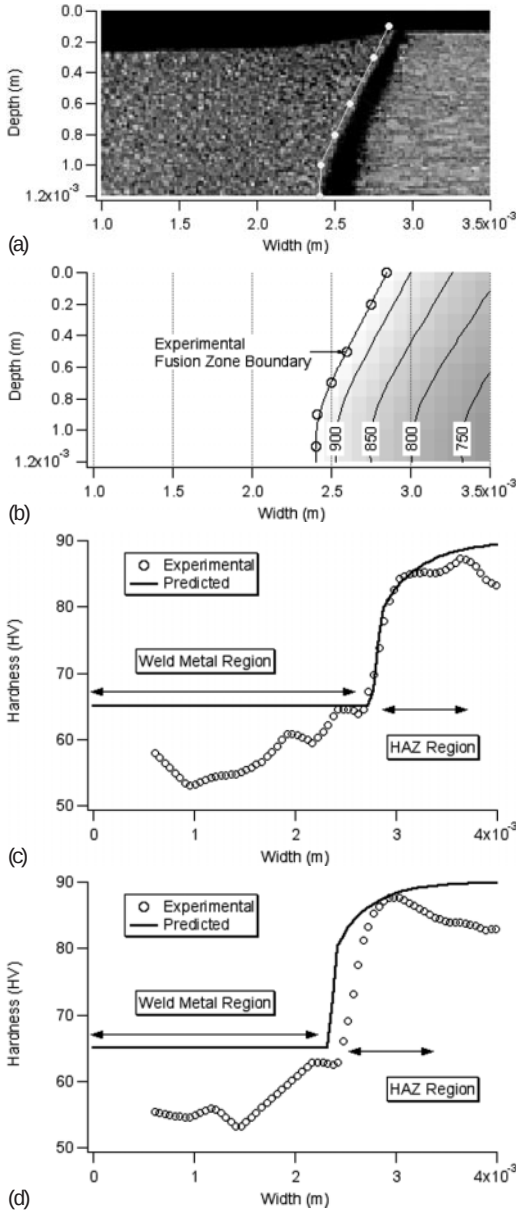

a experimentally measured weld pool profile shown on selected region of 6111 GTA weld; *b* predicted maximum temperature distribution using coupled analytical approach for same conditions as in *a*; *c* direct comparison of predicted and experimental hardness near surface of weld; *d* direct comparison of predicted and experimental hardness at ~1 mm depth from surface of weld

16 Results of HAZ model

(Fig. 16*b*). The temperature distributions follow the weld pool geometry because the model allows for heat transfer only along the width of the sheet.

3. Weld thermal cycles were calculated using the method described above and were used to predict the hardness values using the HAZ microstructure model. The predicted hardness distributions were compared with experimental values at the surface (*see* Fig. 16*c*) and at 1 mm depth from the surface (*see* Fig. 16*d*).

The predictions agreed well with the experimentally measured values. There are small differences between the predicted and experimental hardness distributions. The predicted hardness distribution at 1 mm depth does not follow the shape of the experimental distribution. This is because of the assumption that heat transfer occurs only along the width of the sheet in the present model and the

hardness distribution is anchored to the fusion boundary. In typical welds, the heat transfer occurs along the width and thickness of the sheet. The small errors in the predictions at certain depths from the surface of the sheets were found to be acceptable for process optimisation. Because the present microstructure model cannot describe the WM hardness, a fixed weld metal hardness of 65 HV0·1 was used in the calculations. The important conclusion of the present work is the ability of this coupled model to predict the rapid reduction of hardness in the HAZ.

SUMMARY AND CONCLUSIONS

Welding studies were performed on non-age hardenable 5754 and age hardenable 6111 alloys.

The 5754 alloy was welded without cracking using GTA, EB, and GMA welding processes. In these welds, no significant grain growth was observed in the HAZ regions. The hardness values were similar to those of the base metal regions. The results indicated that the transverse tensile properties are not sensitive to process variations and modelling of thermal behaviour, microstructure, and properties was unnecessary. However, this result is valid only for the transverse properties and further work is necessary to evaluate the longitudinal weld properties.

In all the 6111 alloy welds, hardness measurements showed that WM and HAZ regions were softer than the base metal. Tensile tests also indicated that the strengths of these weldments were lower than that of the base metal.

Thermodynamic and diffusion controlled solidification calculations were applied to predict the phase evolution and the freezing range in the WM region as a function of composition and cooling rate. The calculations indicated an extended freezing range for the 6111 alloys compared with that of the 4047 alloys. Such an extended freezing range corresponds to a higher potential for weld solidification cracking, which was supported by the weld solidification cracking observed during GTA and EB welding. In contrast, the 4047 alloys showed a narrow freezing range and thus a lower tendency for weld solidification cracking. This is supported by the absence of weld cracking in GMA welds in 6111 alloys produced using 4047 filler wire.

For the 6111 alloy welds, a simplified methodology was developed to predict HAZ thermal cycles as a function of the experimentally measured weld pool geometry. The hardness distributions in these welds were predicted using a published model and thermal cycles predicted by a simplified thermal model. The calculated HAZ hardness distributions from the model were in agreement with experimental measurements and showed a rapid hardness reduction near the WM/HAZ boundary.

ACKNOWLEDGEMENTS

The Laboratory Directed Research and Development Program of Oak Ridge National Laboratory sponsored the major part of this research. The Division of Materials Sciences and Engineering, US Department of Energy, sponsored the remainder of this research under contract DE–AC05–00OR22725 with University of Tennessee-Battelle, LLC. The authors thank Alcan International and Reynolds Metals company for providing the aluminium alloys used in this investigation. The authors thank Drs B. Radhakrishnan and S. Agnew of ORNL for helpful discussions.

REFERENCES

1. D. G. ALTENPOHL: 'Aluminum: technology, applications, and environment, a profile of modern metal'; 1998, Warrendale, PA, The Aluminum Association/The Minerals, Metals, and Materials Society.
2. G. B. BURGER, A. K. GUPTA, P. W. JEFFREY, and D. J. LLOYD: *Mater. Charact.*, 1995, **35**, 23–39.
3. A. K. GUPTA, D. J. LLOYD, and M. J. BULL: Proc. 1996 SAE Conf. on 'Development in aluminum use for vehicle design'; SAE Technical Paper Series SP–1164, Paper 960164, Society of Automotive Engineers, Warrendale, PA, 1996.
4. R. P. MARTUKANITZ, B. ALTSHULLER, F. G. ARMAO, and E. R. PICKERING: Proc. 1996 SAE Conf. on 'Development in aluminum use for vehicle design'; SAE Technical Paper Series SP–1164, Paper 960168, Society of Automotive Engineers, Warrendale, PA, 1996.
5. W. A. BAESLACK III, D. D. HARWIG, and J. C. LIPPOLD: 'Weldability testing of Al–Mg–Si alloys', Research Report MR9007, Edison Welding Institute, Columbus, OH, 1990.
6. H. SMARTT: 'A multi-laboratory co-operative and development program', unpublished work, Idaho National Engineering and Environment Laboratory, Idaho Falls, ID, 1998.
7. R. P. WALDUCK and J. BIFFING: *Weld. Met. Fabr.*, 1994, **62**, 172–175.
8. S. A. DAVID, P. FUERSCHBACH, and H. SMARTT: 'A multi-laboratory cooperative research and development program', unpublished research, Oak Ridge National Laboratory, Oak Ridge, TN, 1998.
9. D. ROSENTHAL: *Weld. J.*, 1941, **20**, 220.
10. D. ROSENTHAL: *Trans. ASME*, 1946, **68**, 849.
11. N. N. RYKALIN: 'Berechnug der Wärmevorgänge beim Schweissen'; 1957, Berlin, Verlag Technik.
12. M. F. ASHBY and K. E. EASTERLING: *Acta Metall.*, 1982, **30**, 1969–1978.
13. J. C. ION, K. E. EASTERLING, and M. F. ASHBY: *Acta Metall.*, 1984, **32**, 1949–1962.
14. J. C. ION, H. R. SHERCLIFF, and M. F. ASHBY: *Acta Metall. Mater.*, 1992, **40**, 1539–1551.
15. S. KOU and D. K. SUN: *Metall. Trans. A*, 1985, **16A**, 203.
16. T. ZACHARIA, S. A. DAVID, J. M. VITEK, and T. DEBROY: *Weld. J.*, 1989, **68**, 499s.
17. T. ZACHARIA, S. A. DAVID, J. M. VITEK, and T. DEBROY: *Weld. J.*, 1989, **68**, 510s.
18. K. MUNDRA, T. DEBROY, S. S. BABU, and S. A. DAVID: *Weld. J.*, 1997, **76**, 163s–171s.
19. J. GOLDAK, A. CHAKRAVARTI, and M. BIBBY: *Metall. Trans. B*, 1984, **15B**, 299–305.
20. R. P. MARTUKANITZ: Proc. Int. Conf. on 'Trends in welding research', Gatlinburg, TN, May 1986, ASM International, 193–201.
21. O. R. MYHR and Ø. GRONG: *Acta Metall. Mater.*, 1991, **39**, 2693–2702.
22. O. R. MYHR and Ø. GRONG: *Acta Metall. Mater.*, 1991, **39**, 2703–2708.
23. H. R. SHERCLIFF and M. F. ASHBY: *Acta Metall. Mater.*, 1990, **38**, 1789–1802.
24. H. R. SHERCLIFF and M. F. ASHBY: *Acta Metall. Mater.*, 1990, **38**, 1803–1812.
25. S.-W. CHEN and C.-C. HUANG: *Acta Mater.*, 1996, **44**, 1955–1965.
26. J. L. MURRAY: *Int. Met. Rev.*, 1985, **30**, (5), 211–233.
27. B. SUNDMAN, B. JANSSON, and J. O. ANDERSSON: *Calphad*, 1985, **9**, 153–190.
28. K. HSIEH, S. S. BABU, S. A. DAVID, and J. M. VITEK: *Mater. Sci. Eng. A*, 1996, **A215**, 84–91.
29. J.-O. ANDERSSON, L. HÖGLUND, B. JÖNSSON, and J. ÅGREN: 'Fundamentals and application of ternary diffusion', (ed. G. R. Purdy), 153; 1990, New York, Pergamon.
30. J. ÅGREN: *ISIJ Int.*, 1992, **32**, 291–296.
31. B. RADHAKRISHNAN and T. ZACHARIA: *Metall. Mater. Trans. A*, 1995, **26A**, 2123–2130.
32. S. A. DAVID and J. M. VITEK: *Int. Mater. Rev.*, 1989, **34**, (5), 213–245.
33. A. R. E. SINGER and P. H. JENNINGS: *J. Inst. Met.*, 1947, **73**, 197–212.
34. J. C. BORLAND: *Br. Weld. J.*, 1960, **7**, 508–512.
35. F. MATSUDA, H. NAKAGAWA, and K. SARADA: *Trans. JWRI*, 1982, **11**, 67–77.
36. S. S. BABU and S. A. DAVID: unpublished research, Oak Ridge National Laboratory, Oak Ridge, TN, 1999.
37. Z. FENG, S. A. DAVID, T. ZACHARIA, and C. L. TSAI: *Sci. Technol. Weld. Joining*, 1997, **2**, (1), 11–19.